Letter | Editors' Suggestion

Electron and hole doping of monolayer WSe_2 induced by twisted ferroelectric hexagonal boron nitride

J. Fraunié,[1] R. Jamil,[1] R. Kantelberg,[1] S. Roux,[1] L. Petit,[1] E. Lepleux,[2] L. Pacheco,[2] K. Watanabe,[3] T. Taniguchi,[4] V. Jacques,[5] L. Lombez,[1] M. M. Glazov,[6] B. Lassagne,[1] X. Marie,[1] and C. Robert[1,*]

[1]*Université de Toulouse, INSA-CNRS-UPS, LPCNO, 135 Avenue Rangueil, 31077 Toulouse, France*

[2]*CSI Instruments, 17 Avenue des Andes, 91940 Les Ulis, France*

[3]*International Center for Materials Nanoarchitectonics, National Institute for Materials Science, 1-1 Namiki, Tsukuba 305-00044, Japan*

[4]*Research Center for Functional Materials, National Institute for Materials Science, 1-1 Namiki, Tsukuba 305-00044, Japan*

[5]*Laboratoire Charles Coulomb, Université de Montpellier and CNRS, 34095 Montpellier, France*

[6]*Ioffe Institute, 26 Polytechnicheskaya, 194021 Saint Petersburg, Russia*

(Received 22 October 2023; accepted 5 December 2023; published 27 December 2023)

For the past few years, two-dimensional (2D) ferroelectric materials have attracted strong interest for their potential in future nanoelectronics devices. The recent discovery of 2D ferroelectricity in twisted layers of insulating hexagonal boron nitride, one of the most used 2D materials, has opened the route to its integration into complex van der Waals heterostructures combining hybrid properties. Here we show that opposite polarizations in ferroelectric domains of a folded *h*BN layer can imprint local *n* and *p* doping in a semiconducting transition metal dichalcogenide WSe_2 monolayer. We demonstrate that WSe_2 can be used as an optical probe of ferroelectricity in *h*BN and show that the doping density and type can be controlled with the position of the semiconductor with respect to the ferroelectric interface. Our results establish the ferroelectric *h*BN/WSe_2 van der Waals stacking as a promising optoelectronic structure.

DOI: 10.1103/PhysRevMaterials.7.L121002

The spectacular interest for 2D materials for the past decade has been mainly triggered by the large platform they opened for the design of new structures with combined properties. Indeed, the class of 2D materials now extends to various 2D semiconductors, insulators, metals, magnets, superconductors, topological insulators, etc. Stacking of these 2D materials into so-called van der Waals (vdW) heterostructures has opened a route toward the design of complex hybrid structures combining 2D materials with radically different properties [1]. Beyond combining the individual properties of both materials in the same structure they also enable a mutual control of these properties through proximity effects at the interface. Among the various 2D hybrid structures that have been reported for the past few years, monolayers (MLs) of semiconducting transition metal dichalcogenide (TMD) such as MoS_2 or WSe_2 often play an important role due to their peculiar optical and spin properties. For instance, these materials have been coupled to 2D magnets [2,3] to study magnetic proximity effects or with graphene to induce spin-orbit coupling [4].

Recently, the class of 2D materials has been extended with the discovery of 2D ferroelectricity [5]. The integration of 2D ferroelectrics (FEs) with 2D semiconductors (SCs) is interesting from several perspectives. First, it can be used for the design of electronic devices such as ferroelectric field effect transistors (FeFET) [6]. Second, it can open new strategies to implement optoelectronic properties. For instance, electric fields induced by the 2D FE can be used to locally tune the optical properties and the doping density of the 2D SC. It can also pave the way toward the optical control of FE properties to address FE-based memories. While many studies have reported the integration of TMD materials with standard bulk [three-dimensional (3D)] FE materials such as $BiFeO_3$ for the purpose of electronic devices [7–9], the literature on the optical properties of 3D FE/TMD heterostructures is much scarcer. The reason is that these structures suffer from one main drawback: the 3D nature of the FE materials degrades the optical quality of the overlying TMD layer due to the presence of dangling bonds. A fully 2D FE/TMD hybrid vdW heterostructure is thus in high demand. While a few 2D materials (SnTe, $CuInP_2S_6$, etc.) exhibit intrinsic ferroelectricity due to their distorted crystal structure [10,11], their integration with TMD layers has been mostly limited to the demonstration of FeFET prototypes [12,13]. Very few studies have dealt with the optical properties of 2D FE/TMD heterostructures. Mao *et al.* demonstrated hysteretic optical properties in a $MoSe_2/CuInP_2S_6$ gated device [14] while Li *et al.* recently measured the optical properties of a $MoS_2/CuInP_2S_6$ stacking but observed a strong quenching of the luminescence of MoS_2 due to the semiconducting nature of $CuInP_2S_6$ [15]. In summary, finding a 2D FE material that can tune but not degrade the optical properties of the TMD layer would thus constitute a major breakthrough in the field.

Hexagonal boron nitride (*h*BN) is a 2D insulator that has been extensively used to encapsulate TMD MLs and strongly enhance their optical properties [16,17]. In its bulk form, *h*BN is not ferroelectric, but recently it has been

*cerobert@insa-toulouse.fr

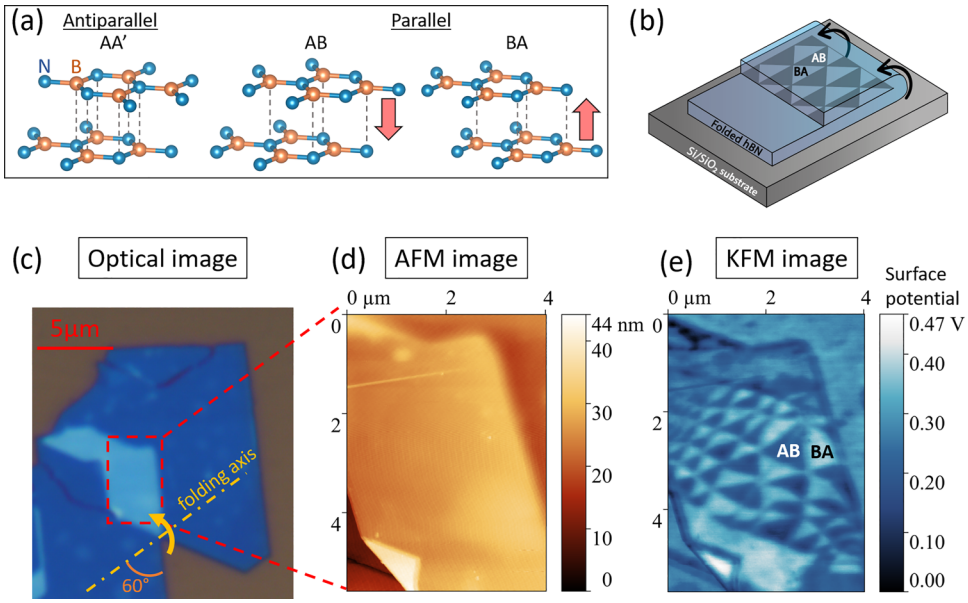

FIG. 1. (a) Stable stacking arrangements for antiparallel and parallel alignment. The AA′ stacking is the configuration in bulk *h*BN. For parallel alignment, only AB and BA stacking are stable and exhibit out-of-plane electric polarization marked by the red arrows. (b) Sketch of a folded *h*BN flake. Triangular AB and BA ferroelectric domains are present at the folded interface. (c)–(e) Optical, AFM, and KFM images of a *h*BN flake folded along an armchair axis.

demonstrated that ferroelectricity can occur at the interface between marginally twisted *h*BN layers close to a parallel alignment [18–21] opening the field of sliding ferroelectricity [22–24]. Promising theoretical works have predicted that the electric potential of twisted *h*BN can be imprinted in a TMD ML [25], resulting in large shifts of the band edges in the SC. Very recently, Kim *et al.* observed a change in the exciton diffusion in a $MoSe_2$ ML attributed to the proximity of a twisted *h*BN interface [26]. In this Letter, we demonstrate experimentally that the presence of a FE-*h*BN interface with out-of-plane up and down polarized domains locally imprints electron and hole doped regions in the plane of a WSe_2 ML. In addition, we calculate the electric stray field induced by the FE interface and discuss its role in the doping mechanism and possible dissociation of excitons in the WSe_2 ML. Our results establish a strategy to locally dope TMD layers, change their optical properties without using external metallic gates, and more generally highlight the potential of FE-*h*BN/TMD heterostructures for the design of original optoelectronics properties.

Out-of-plane electric polarization can be created when two layers of *h*BN are artificially aligned in a parallel configuration with a twist angle close to 0°. Such a stacking generally results in reconstructed triangular domains with stable AB and BA arrangement that exhibit perpendicular dipoles with up and down electric polarization [see Fig. 1(a)]. In the previous studies, two main techniques have been used to fabricate these stacking. Yasuda *et al.* used the "tear-and-stack" technique to pick up one half of a *h*BN monolayer flake and transfer it on top of the remaining half [20]. Vizner Stern *et al.* used a very similar technique but on a slightly thicker flake (1–5 nm), showing that the observation of ferroelectricity is not limited to twisted bilayers [19]. Finally, Woods *et al.* stacked two *h*BN flakes that were adjacently exfoliated on a SiO_2/Si substrate assuming that they originated from the same growth domain and are thus nearly perfectly aligned [21]. Intentional or unintentional folding of 2D layers has been successfully used to create a moiré pattern [27–29]. In our work, we show that we can obtain FE-*h*BN in a simple way by selecting thin *h*BN flakes that are accidentally folded during the exfoliation process. Figure 1(c) shows an optical image of a thin *h*BN flake (∼13 nm) that was exfoliated using the Scotch tape technique on a SiO_2(80nm)/Si surface (see details in the Supplemental Material [30]; also see Refs. [31–33]). We clearly see a dark blue region corresponding to the thinnest part of the flake and a light blue region corresponding to a thicker part. The light blue region corresponds to the same thin flake that has been folded probably during the exfoliation process [34]. Interestingly, we clearly see that the edges of the folded part make a perfect 60° angle that are likely representing either zigzag or armchair crystallographic axes of *h*BN [35]. In addition, we note that the angles between the folding axis and the edges of the flake are also 60° so that these three directions correspond to the same configuration (they are either all zigzag or all armchair). We show in the Supplemental Material [30] that folding along a zigzag (armchair) axis necessarily corresponds to an antiparallel (parallel) alignment of the two *h*BN layers at the interface. The folded part is then characterized using atomic force microscopy (AFM) and Kelvin probe force microscopy (KFM). The AFM image [Fig. 1(d)] shows that the top surface of the flake is atomically flat. The KFM image [Fig. 1(e)] shows triangular regions with two distinct surface potentials that are characteristic of a parallel alignment and ferroelectric domains with AB and BA atomic arrangement at the interface between the two folded parts of the flakes [19–21]. This demonstrates that the folding axis in this flake is along an armchair direction. The potential difference between bright and dark domains is 150 ± 20 mV, in agreement with previous studies [19–21]. The typical size of domains varies from 100 nm to 1 µm on this flake. Other examples of folded

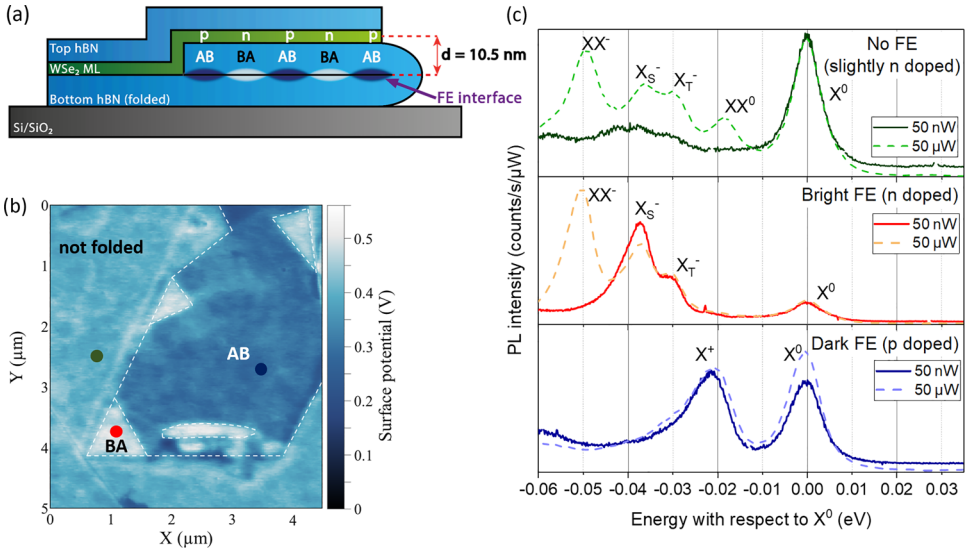

FIG. 2. (a) Sketch of the FE-*h*BN/WSe_2 ML/*h*BN van der Waals heterostructure. (b) KFM image of the folded bottom *h*BN flake. Bright (BA) and dark (AB) are clearly observed. White dashed lines show the borders of the ferroelectric domains. (c) PL spectra at three typical positions of the sample marked by the colored points in (b). Measurements are performed at $T = 55$ K and for two extreme excitation powers of 50 μW and 50 nW. For a given position, we divide the intensity by the integration time and the excitation power. Spectra are plotted as a function of the energy with respect to the bright neutral exciton X^0 peak to correct from energy shift of the whole spectra due to inhomogeneous strain.

flakes exhibiting small triangular domains are shown in the Supplemental Material [30]. This first result demonstrates that we can easily obtain FE domains using a single step mechanical exfoliation technique by selecting self-folded flakes. Beyond its simplicity as compared to the stacking methods previously reported in the literature [19–21], this technique can potentially create very large domains exceeding the micrometer size. Figure 2(b) shows the KFM image of another folded *h*BN flake with similar surface potential contrast but with larger area. Other examples are shown in Fig. 4(b) and in the Supplemental Material [30]. In the following, we will use such *h*BN flakes with large domains to optically probe in-plane doping modulation in TMD ML in close proximity.

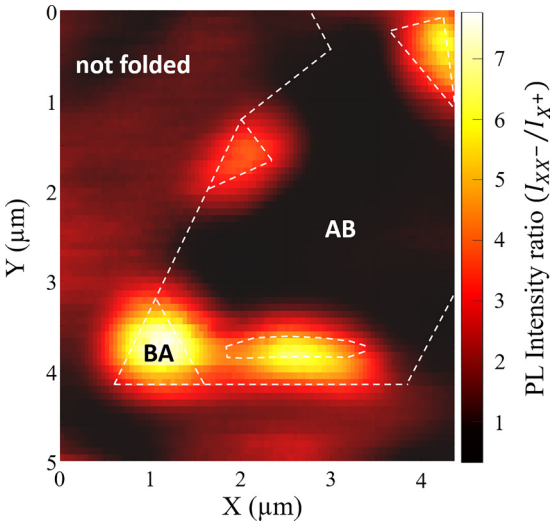

FIG. 3. Ratio of PL intensities of the negatively charged biexciton I_{XX^-} and positive trion I_{X^+} for the heterostructure presented in Fig. 2. The borders of the ferroelectric domains observed in the KFM image of Fig. 2(b) are reproduced by white dashed lines.

Figure 2(a) shows a sketch of the studied structure. A WSe_2 ML is transferred on top of the folded *h*BN flake with large FE domains and capped with a thin (not folded) *h*BN flake (see the fabrication details in the Supplemental Material [30]). The distance between the WSe_2 ML and the FE interface is simply given by the thickness of the folded part (10.5 nm for this sample). We checked that the transfer of the WSe_2 ML and the top *h*BN flake does not significantly affect the size of the FE domains by performing KFM measurements at each step of the fabrication (see Supplemental Material [30]). We then perform microphotoluminescence (PL) measurements on the WSe_2 ML. Importantly, the diameter of the optical spot is limited by diffraction (∼500 nm) but is smaller than the size of the FE domains so we can measure the PL of WSe_2 on top of a *bright* or a *dark FE* domain separately (here *bright* and *dark FE* domains refer to the KFM image of Fig. 2(b) that we attribute to BA and AB stacking). Figure 2(c) presents typical PL spectra taken at three positions of the sample (on a bright FE domain, a dark FE domain, and on the unfolded part of the *h*BN flake showing no FE domain). Measurements are shown at 55 K and for two excitation powers of 50 nW and 50 μW. We recall in the Supplemental Material [30] the configurations of the different excitonic complexes that are observed in these spectra. We use the energy splitting of the peaks with respect to the bright neutral exciton and the power dependence of their intensity to identify the nature of the excitonic transitions in accordance with the literature [36,37]. The key observations in Fig. 2(c) are the following:

(1) The PL spectrum on the no FE area is characteristic of an intrinsically slightly *n*-doped WSe_2 ML [36,37]. At low excitation power (50 nW), we observe mainly the peak labeled

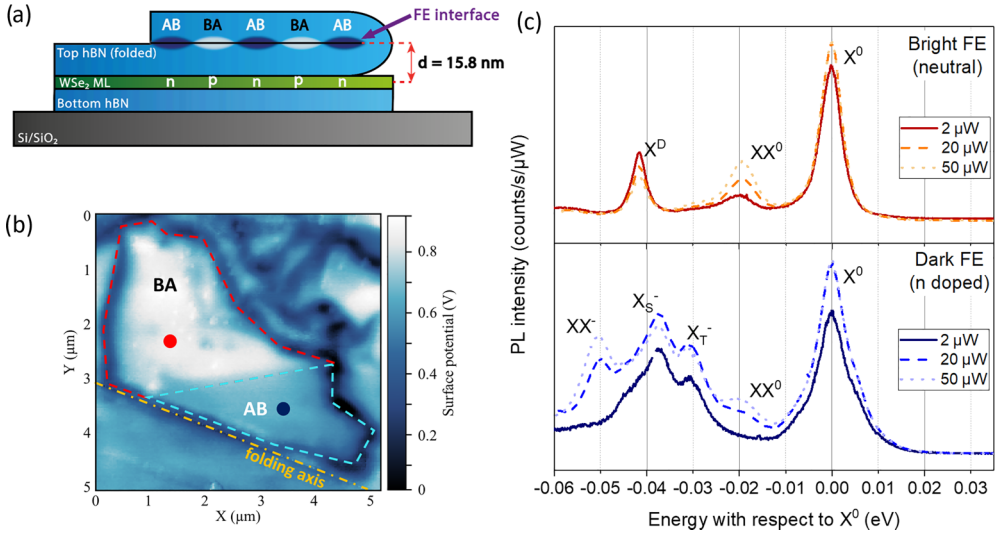

FIG. 4. (a) Sketch of the *h*BN/WSe_2 ML/FE-*h*BN van der Waals heterostructure. (b) KFM image of the final structure. Bright (BA) and dark (AB) are highlighted with red and blue dashed lines. Optical and AFM images are presented in the Supplemental Material [30]) Typical PL spectra on both bright and dark ferroelectric domains are marked by the colored points in (b). Measurements are performed at $T = 55$ K and for three excitation powers of 2, 20, and 50 μW. For a given position, we divide the intensity by the integration time and the excitation power. Spectra are plotted as a function of the energy with respect to the bright neutral exciton X^0 peak to correct from energy shift of the whole spectra due to inhomogeneous strain.

X^0 that corresponds to the bright neutral exciton. At an energy 18 meV below X^0 we observe the neutral biexciton (XX^0) that can only be seen at high excitation power (50 μW). The two negative bright trions (triplet X_T^- and singlet X_S^-) are observed 29 and 36 meV below X^0. Finally, the negatively charged biexciton (XX^-) is observed 51 meV below X^0 only at high excitation power. These negatively charged exciton complexes (X_T^-, X_S^-, and XX^-) can only be seen if the WSe_2 ML is *n* doped.

(2) The PL spectrum on the bright FE domains shows the same peaks but with intensities that are characteristic of a larger *n* doping. Indeed, the intensity of the neutral transitions (X^0 and XX^0) is reduced as compared to the no FE spectra while the intensity associated with negatively charged excitonic complexes (X_T^-, X_S^- and XX^-) is enhanced.

(3) The PL spectrum on the dark FE domain is radically different. The negatively charged excitonic complexes are absent. On the opposite, we observe a peak 21 meV below X^0 at both high and low excitation powers. This peak is attributed to the positive bright trion (X^+) indicating a *p* doping of the WSe_2 ML.

The results of Fig. 2 clearly show that the FE domains in the bottom *h*BN flake control the nature of the doping in the WSe_2 ML (*n* doping in bright FE domain versus *p* doping in the dark FE domain). In Fig. 3, we show that the WSe_2 ML can be used to optically image the FE domains in *h*BN. By moving the sample with a piezo-driven scanner, we record the PL spectrum at each point of the WSe_2 ML. Measurements are performed at 55 K for an excitation power of 20 μW. For each pixel, we plot the ratio between the intensity of the negatively charged biexciton (I_{XX^-}) that is a signature of *n* doping and the intensity of the positive trion (I_{X^+}) that is a signature of *p* doping. We choose these two transitions because they are spectrally well separated. More details about the data analysis can be found in the Supplemental Material [30]. We clearly see that the PL ratio I_{XX^-}/I_{X^+} is large (small) in the bright (dark) FE domains shown in the KFM image of Fig. 2(b). These results confirm that FE domains in *h*BN imprint *n*/*p* domains in the WSe_2 ML.

We now show that the type (*p*/*n*) and the density of doping can be controlled with the position of the WSe_2 ML with respect to the FE-*h*BN interface. Figure 4(a) shows the sketch of a second heterostructure where a folded *h*BN flake with FE domains is transferred onto a WSe_2 ML while the bottom *h*BN flake is not folded. The distance between the FE interface and the WSe_2 ML is larger than in the structure presented in Fig. 2 (15.8 nm). Figure 4(b) shows the KFM image of the final structure. Although the FE domains are significantly affected by the transfer process, we can identify two large FE domains with opposite polarization in the top *h*BN flake. Figure 4(c) presents the PL spectra of the WSe_2 ML in both regions. The dark domain in the KFM image now corresponds to a *n*-doped WSe_2. This is opposite to the results of Fig. 2 but perfectly consistent with the direction of the electric field in the WSe_2 ML; i.e., in Fig. 2 the FE-*h*BN is below the WSe_2 while it is above it in Fig. 4. The PL spectrum taken on the bright FE domain is typical of a nearly neutral WSe_2 ML where charged excitonic complexes are absent and only neutral transitions (bright exciton X^0, biexciton XX^0, and dark exciton X^D) are visible. Given that the WSe_2 ML is intrinsically slightly *n* doped, we conclude that the effect of the bright FE domain is to slightly compensate the doping with holes. The results of Fig. 4 demonstrate that the 2D SC layer can feel the influence of the FE-*h*BN at a distance as large as 15 nm but with a *p*/*n* modulation that is smaller than the modulation observed in the structure of Fig. 2. This could be due to the larger distance between the FE-*h*BN interface and the WSe_2 ML, and shows that the doping density in WSe_2 can potentially be tuned with the thickness of the folded *h*BN flake. Nevertheless, further studies are required to properly separate the effect of the

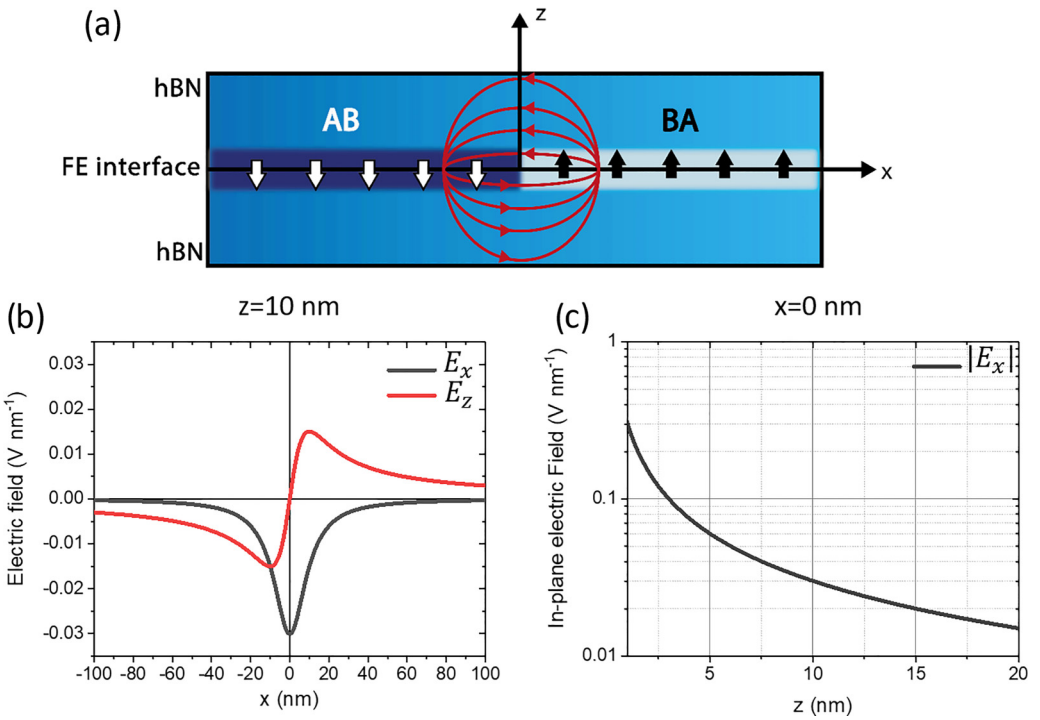

FIG. 5. (a) Sketch of the structure used for the calculation of the electric stray field (red lines). We consider two semi-infinite planes with dipole moment density $+P_0$ (black arrows) and $-P_0$ (white arrows) separated by an infinitely small domain wall at $x = 0$. We use $P_0 = 2\,\mathrm{pC.m^{-1}}$ [18]. We consider that the medium surrounding the FE interface is *h*BN with relative permittivity $\varepsilon_r = 3$. (b) Calculated components of the electric field at a distance $z = 10$ nm above the FE interface. (c) Absolute value of the in-plane electric field as a function of z and for $x = 0$ nm.

*h*BN thickness on the doping density from possible extrinsic parameters such as strain, contamination, or defect density in the ML.

While our results clearly demonstrate a local modulation of the doping from *n* type to *p* type in the WSe_2 ML, they raise the question about the origin of the free charge carriers. Indeed, despite its FE interface, *h*BN remains an insulator and it is unlikely that charge transfer occurs between WSe_2 and *h*BN. Possible piezoelectric effects in our structure due to local strain seem to be unlikely owing to reduced strain in the WSe_2 and weak piezoelectricity in multilayers of *h*BN. A possibility is that the electric stray field induced by the FE interface favors the release of charges that are trapped in the WSe_2 ML or in close proximity, e.g., at the interface with *h*BN. This scenario is consistent with the temperature dependence of the doping density in our FE-*h*BN/WSe_2 heterostructure (see Supplemental Material [30]). When the sample is cooled down to 5 K, the modulation of the doping between bright and dark FE domains occurs but is reduced as compared to the results of Fig. 2 shown at 55 K. Both thermal energy and electric field may contribute to the release of trapped charges.

Another possibility is that *n*-doped and *p*-doped regions result from the combination of light excitation and in-plane electric field. Indeed, light excitation of the WSe_2 ML generates electron-hole pairs that bind to form neutral excitons with a significant binding energy (around 170 meV [38] for a WSe_2 ML encapsulated into *h*BN). These excitons can dissociate only under a large in-plane electric field. In FE-*h*BN domains, the direction of the electric field is out of plane. Nevertheless, the stray electric field that is present in the WSe_2 ML above or below a FE domain wall is necessarily in plane [25]. Depending on the distance between the FE interface and the ML, the amplitude of this in-plane electric stray field may be enough to partially dissociate excitons that are created in the vicinity of the domain wall so that free electrons and free holes accumulate on each side. These free charges can then bind to neutral excitons that are photogenerated in the domains to form the charged excitonic complexes observed in Figs. 2(c) and 4(c).

In both scenarios, the role of the electric stray field is crucial. It is thus important to estimate its amplitude using a simple model based on Maxwell equations. We calculate the electric field induced by a FE domain wall caused by the two stackings AB and BA [see the sketch in Fig. 5(a)]. We assume that the FE interface is in the (xy) plane and is surrounded by a homogeneous medium of *h*BN (not ferroelectric) with permittivity ε. For simplicity, we assume that the domain wall is infinitely small at $x = 0$ and do not take into account any in-plane polarization around the domain wall [39]. We consider two semi-infinite domains of opposite dipole moment density $\pm P_0$ parallel to the z axis. This assumption is realistic as the size of the domains in our samples is much larger than the distance between the FE interface and the WSe_2 ML. We can show (see Supplemental Material [30] for calculation details) that the electric field components are

$$E_x = -\frac{4P_0}{\varepsilon}\frac{z}{x^2+z^2},\ E_y = 0,\ E_z = \frac{4P_0}{\varepsilon}\frac{x}{x^2+z^2}.$$

Figure 5(b) presents both in-plane (E_x) and out-of-plane (E_z) components as a function of x for a distance $z = 10$ nm corresponding to the position of the WSe_2 ML in the sample presented in Fig. 2. As expected, the electric field is strictly in plane just above the domain wall ($x = 0$) whereas the out-of-plane component varies from positive to negative while crossing the domain wall. The maximum in-plane electric field is $30\,\mathrm{mV.nm^{-1}}$. This is comparable to a typical external electric field used in photocurrent measurements that evidenced exciton dissociation in WSe_2 [40] and not far from the theoretical value of $50\,\mathrm{mV.nm^{-1}}$ corresponding to equal dissociation rate and the intrinsic decay rate of the exciton in hBN/MoS_2/hBN [41]. Moreover, it was shown recently that 10% of excitons can spontaneously dissociate into electron-hole pairs due to interaction with defects [42]. The in-plane electric field present in our samples could thus assist the separation of electrons and holes into separate domains. Finally, the in-plane electric field may also favor dissociation of the excited states of excitons with smaller binding energy. In summary, our calculations prove that exciton dissociation at the domain wall must be considered as a possible mechanism for creating the charges. It is also important to note that both electric field components vanish for $x \to \infty$. This means that the electric stray field is almost zero in the WSe_2 ML located at the center of the domains. To the contrary, the results of Fig. 3 show that large areas of WSe_2 are charged and not only the surrounding of the domain walls. This proves that whatever the mechanism that creates these charges, diffusion occurs on distances as long as the domain size. Moreover, it is important to note that in our samples the WSe_2 ML is not connected to any electrode so that accumulated charges in separate domains cannot be easily evacuated.

Finally, we present in Fig. 5(c) the amplitude of the maximum in-plane electric field (at $x = 0$) as a function of z. It clearly shows that reducing the distance between the WSe_2 ML and the FE interface, i.e., reducing the thickness of hBN down to a few layers, should strongly enhance the electric field in the range of a few hundreds of $\mathrm{mV.nm^{-1}}$. Such a field is difficult to obtain with external electrodes and it would be interesting from many perspectives where efficient dissociation of excitons is needed, including photodetector, photovoltaics, photocatalysis, and other applications.

In summary, we have shown that parallel alignment can occur when a hBN flake is folded along one of its armchair axes resulting in ferroelectric domains at the interface. We then demonstrated that ferroelectric hBN can imprint in-plane p/n charge carrier domains in a WSe_2 ML. Such heterostructures could be used in the near future for several applied and fundamental perspectives. Original architectures of LED or photodetectors can be built by depositing electric contacts on both p and n regions. Besides exciton dissociation, the combination of p/n doping in the TMD and the in-plane electric field in the vicinity of a domain wall may result in the localization of one-dimensional excitons similar to the recent results of Thureja *et al.* [43] using external gates. Further nontrivial localization effects may also occur at the apexes of the triangular domains. Finally, our results should stimulate future studies on possible optical switching of the FE polarization in hBN using photogenerated excitons in a TMD structure as was demonstrated in 3D-FE/MoS_2 [44].

We thank T. Amand for fruitful discussions. This work was supported by Agence Nationale de la Recherche funding under the program ESR/EquipEx+ (Grant No. ANR-21-ESRE-0025); ANR ATOEMS and ANR IXTASE, through Grant No. NanoX ANR-17-EURE-0009 in the framework of the "Programme des Investissements d'Avenir"; and by the Institute for Quantum Technologies in Occitanie through Project 2D-QSens. K.W. and T.T. acknowledge support from the Elemental Strategy Initiative conducted by MEXT, Japan and CREST (Grant No. JPMJCR15F3), JST. X.M. also acknowledges the Institut Universitaire de France.

[1] A. K. Geim and I. V. Grigorieva, Van der Waals heterostructures, Nature (London) **499**, 419 (2013).

[2] D. Zhong, K. L. Seyler, X. Linpeng, R. Cheng, N. Sivadas, E. Schmidgall, T. Taniguchi, K. Watanabe, M. A. McGuire, W. Yao *et al.*, Van der Waals engineering of ferromagnetic semiconductor heterostructures for spin and valleytronics, Sci. Adv. **3**, e1603113 (2017).

[3] L. Ciorciaro, M. Kroner, K. Watanabe, T. Taniguchi, and A. Imamoglu, Observation of magnetic proximity effect using resonant optical spectroscopy of an electrically tunable $MoSe_2$/$CrBr_3$ heterostructure, Phys. Rev. Lett. **124**, 197401 (2020).

[4] A. Avsar, J. Y. Tan, T. Taychatanapat, J. Balakrishnan, G. K. W. Koon, Y. Yeo, J. Lahiri, A. Carvalho, A. S. Rodin, E. C. T. O'Farrell *et al.*, Spin–orbit proximity effect in graphene, Nat. Commun. **5**, 4875 (2014).

[5] Z. Guan, H. Hu, X. Shen, P. Xiang, N. Zhong, J. Chu, and C. Duan, Recent progress in two-dimensional ferroelectric materials, Adv. Electron. Mater. **6**, 1900818 (2020).

[6] C. Zhou and Y. Chai, Ferroelectric-gated two-dimensional-material-based electron devices, Adv. Electron. Mater. **3**, 1600400 (2017).

[7] J. Chen, S. Lo, S. Ho, S. Wong, T. Vu, X. Zhang, Y. Liu, Y. Chiou, Y. Chen, J. Yang *et al.*, A gate-free monolayer WSe_2 pn diode, Nat. Commun. **9**, 3143 (2018).

[8] D. Dai, X. Wang, J. Yang, J. Dang, Y. Yuan, B. Fu, X. Xie, L. Yang, S. Xiao, S. Shi *et al.*, Single charge control of localized excitons in heterostructures with ferroelectric thin films and two-dimensional transition metal dichalcogenides, Nanoscale **14**, 14537 (2022).

[9] R. Salazar, S. Varotto, C. Vergnaud, V. Garcia, S. Fusil, J. Chaste, T. Maroutian, A. Marty, F. Bonell, D. Pierucci *et al.*, Visualizing giant ferroelectric gating effects in large-scale WSe_2/$BiFeO_3$ heterostructures, Nano Lett. **22**, 9260 (2022).

[10] F. Liu, L. You, K. L. Seyler, X. Li, P. Yu, J. Lin, X. Wang, J. Zhou, H. Wang, H. He *et al.*, Room-temperature ferroelectricity in $CuInP_2S_6$ ultrathin flakes, Nat. Commun. **7**, 12357 (2016).

[11] K. Chang, J. Liu, H. Lin, N. Wang, K. Zhao, A. Zhang, F. Jin, Y. Zhong, X. Hu, W. Duan *et al.*, Discovery of robust in-plane ferroelectricity in atomic-thick SnTe, Science **353**, 274 (2016).

[12] M. Si, P.-Y. Liao, G. Qiu, Y. Duan, and P. D. Ye, Ferroelectric field-effect transistors based on MoS_2 and $CuInP_2S_6$ two-dimensional van der Waals heterostructure, ACS Nano **12**, 6700 (2018).

[13] X. Jiang, X. Hu, J. Bian, K. Zhang, L. Chen, H. Zhu, Q. Sun, and D. W. Zhang, Ferroelectric field-effect transistors based on $WSe_2/CuInP_2S_6$ heterostructures for memory applications, ACS Appl. Electron. Mater. **3**, 4711 (2021).

[14] X. Mao, J. Fu, C. Chen, Y. Li, H. Liu, M. Gong, and H. Zeng, Nonvolatile electric control of exciton complexes in monolayer $MoSe_2$ with two-dimensional ferroelectric $CuInP_2S_6$, ACS Appl. Mater. Interfaces **13**, 24250 (2021).

[15] P. Li, A. Chaturvedi, H. Zhou, G. Zhang, Q. Li, J. Xue, Z. Zhou, S. Wang, K. Zhou, Y. Weng *et al.*, Electrostatic coupling in $MoS_2/CuInP_2S_6$ ferroelectric vdW heterostructures, Adv. Funct. Mater. **32**, 2201359 (2022).

[16] F. Cadiz, E. Courtade, C. Robert, G. Wang, Y. Shen, H. Cai, T. Taniguchi, K. Watanabe, H. Carrere, D. Lagarde *et al.*, Excitonic linewidth approaching the homogeneous limit in MoS_2-based van der Waals heterostructures, Phys. Rev. X **7**, 021026 (2017).

[17] O. A. Ajayi, J. V. Ardelean, G. D. Shepard, J. Wang, A. Antony, T. Taniguchi, K. Watanabe, T. F. Heinz, S. Strauf, X-Y Zhu *et al.*, Approaching the intrinsic photoluminescence linewidth in transition metal dichalcogenide monolayers, 2D Mater. **4**, 031011 (2017).

[18] L. Li and M. Wu, Binary compound bilayer and multilayer with vertical polarizations: Two-dimensional ferroelectrics, multiferroics, and nanogenerators, ACS Nano **11**, 6382 (2017).

[19] M. Vizner Stern, Y. Waschitz, W. Cao, I. Nevo, K. Watanabe, T. Taniguchi, E. Sela, M. Urbakh, O. Hod, and M. Ben Shalom, Interfacial ferroelectricity by van der Waals sliding, Science **372**, 1462 (2021).

[20] K. Yasuda, X. Wang, K. Watanabe, T. Taniguchi, and P. Jarillo-Herrero, Stacking-engineered ferroelectricity in bilayer boron nitride, Science **372**, 1458 (2021).

[21] C. R. Woods, P. Ares, H. Nevison-Andrews, M. J. Holwill, R. Fabregas, F. Guinea, A. K. Geim, K. S. Novoselov, N. R. Walet, and L. Fumagalli, Charge-polarized interfacial superlattices in marginally twisted hexagonal boron nitride, Nat. Commun. **12**, 347 (2021).

[22] M. Wu and J. Li, Sliding ferroelectricity in 2D van der Waals materials: Related physics and future opportunities, Proc. Natl. Acad. Sci. USA **118**, e2115703118 (2021).

[23] A. Weston, E. G. Castanon, V. Enaldiev, F. Ferreira, S. Bhattacharjee, S. Xu, H. Corte-León, Z. Wu, N. Clark, A. Summerfield *et al.*, Interfacial ferroelectricity in marginally twisted 2D semiconductors, Nat. Nanotechnol. **17**, 390 (2022).

[24] X. Wang, K. Yasuda, Y. Zhang, S. Liu, K. Watanabe, T. Taniguchi, J. Hone, L. Fu, and P. Jarillo-Herrero, Interfacial ferroelectricity in rhombohedral-stacked bilayer transition metal dichalcogenides, Nat. Nanotechnol. **17**, 367 (2022).

[25] P. Zhao, C. Xiao, and W. Yao, Universal superlattice potential for 2D materials from twisted interface inside *h*-BN substrate, npj 2D Mater. Appl. **5**, 38 (2021).

[26] D. S. Kim, R. C. Dominguez, R. Mayorga-Luna, D. Ye, J. Embley, T. Tan, Y. Ni, Z. Liu, M. Ford, F. Y. Gao *et al.*, Electrostatic moiré potential from twisted hexagonal boron nitride layers, Nat. Mater. (2023).

[27] H. Schmidt, J. C. Rode, D. Smirnov, and R. J. Haug, Superlattice structures in twisted bilayers of folded graphene, Nat. Commun. **5**, 5742 (2014).

[28] J. S. Chang, S. Kim, H.-J. Sung, J. Yeon, K. J. Chang, X. Li, and S. Kim, Graphene nanoribbons with atomically sharp edges produced by AFM induced self-folding, Small **14**, 1803386 (2018).

[29] X. Du, Y. Lee, Y. Zhang, T. Yu, K. Kim, and N. Liu, Electronically weak coupled bilayer MoS_2 at various twist angles via folding, ACS Appl. Mater. Interfaces **13**, 22819 (2021).

[30] See Supplemental Material at http://link.aps.org/supplemental/10.1103/PhysRevMaterials.7.L121002 for experimental methods, details on the determination of the folding axis, pictures of other folded flakes, additional KFM images of the structure shown in Fig. 2, sketches of the excitonic complexes in WSe_2, details on the protocol used for the analysis of the photoluminescence mapping, temperature dependence measurements, and details of the calculation of the electric stray field. It also contains Refs. [31–33].

[31] T. Taniguchi and K. Watanabe, Synthesis of high-purity boron nitride single crystals under high pressure by using Ba-BN solvent, J. Cryst. Growth **303**, 525 (2007).

[32] A. Castellanos-Gomez, M. Buscema, R. Molenaar, V. Singh, L. Janssen, H. S. J. van der Zant, and G. A. Steele, Deterministic transfer of two-dimensional materials by all-dry viscoelastic stamping, 2D Mater. **1**, 011002 (2014).

[33] P. J. Zomer, M. H. D. Guimarães, J. C. Brant, N. Tombros, and B. J. van Wees, Fast pick up technique for high quality heterostructures of bilayer graphene and hexagonal boron nitride, Appl. Phys. Lett. **105**, 013101 (2014).

[34] Y. Jiang, S. Sridhar, Z. Liu, D. Wang, H. Zhou, J. Deng, H. B. Chew, and C. Ke, The interplay of intra- and inter-layer interactions in bending rigidity of ultrathin 2D materials, Appl. Phys. Lett. **122**, 153101 (2023).

[35] Y. Guo, C. Liu, Q. Yin, C. Wei, S. Lin, T. B. Hoffman, Y. Zhao, J. H. Edgar, Q. Chen, S. P. Lau *et al.*, Distinctive in-plane cleavage behaviors of two-dimensional layered materials, ACS Nano **10**, 8980 (2016).

[36] M. Yang, L. Ren, C. Robert, D. Van Tuan, L. Lombez, B. Urbaszek, X. Marie, and H. Dery, Relaxation and darkening of excitonic complexes in electrostatically doped monolayer WSe_2: Roles of exciton-electron and trion-electron interactions, Phys. Rev. B **105**, 085302 (2022).

[37] Z. Li, T. Wang, Z. Lu, C. Jin, Y. Chen, Y. Meng, Z. Lian, T. Taniguchi, K. Watanabe, S. Zhang *et al.*, Revealing the biexciton and trion-exciton complexes in BN encapsulated WSe_2, Nat. Commun. **9**, 3719 (2018).

[38] M. Goryca, J. Li, A. V. Stier, T. Taniguchi, K. Watanabe, E. Courtade, S. Shree, C. Robert, B. Urbaszek, X. Marie *et al.*, Revealing exciton masses and dielectric properties of monolayer semiconductors with high magnetic fields, Nat. Commun. **10**, 4172 (2019).

[39] D. Bennett, G. Chaudhary, R.-J. Slager, E. Bousquet, and P. Ghosez, Polar meron-antimeron networks in strained and twisted bilayers, Nat. Commun. **14**, 1629 (2023).

[40] M. Massicotte, F. Vialla, P. Schmidt, M. B. Lundeberg, S. Latini, S. Haastrup, M. Danovich, D. Davydovskaya, K. Watanabe, T. Taniguchi *et al.*, Dissociation of two-dimensional excitons in monolayer WSe_2, Nat. Commun. **9**, 1633 (2018).

[41] S. Haastrup, S. Latini, K. Bolotin, and K. S. Thygesen, Stark shift and electric-field-induced dissociation of excitons in monolayer MoS_2 and hBN/MoS_2 heterostructures, Phys. Rev. B **94**, 041401(R) (2016).

[42] T. Handa, M. A. Holbrook, N. Olsen, L. N. Holtzman, L. Huber, H. I. Wang, M. Bonn, K. Barmak, J. C. Hone, A. N. Pasupathy *et al.*, Spontaneous exciton dissociation in transition metal dichalcogenide monolayers, arXiv:2306.10814.

[43] D. Thureja, A. Imamoglu, T. Smole'ski, I. Amelio, A. Popert, T. Chervy, X. Lu, S. Liu, K. Barmak, K. Watanabe *et al.*, Electrically tunable quantum confinement of neutral excitons, Nature (London) **606**, 298 (2022).

[44] T. Li, A. Lipatov, H. Lu, H. Lee, J. Lee, E. Torun, L. Wirtz, C. Eom, J. Íñiguez, A. Sinitskii *et al.*, Optical control of polarization in ferroelectric heterostructures, Nat. Commun. **9**, 3344 (2018).